12th International Symposium on Turbulence and Shear Flow Phenomena (TSFP12)
Osaka, Japan (Online), July 19 to 22, 2022

SPECTRAL PROPER ORTHOGONAL DECOMPOSITION OF THE JUNCTION FLOW BEHIND A CANTILEVERED SQUARE CYLINDER

Ali Mohammadi[1], **Chris Morton**[1] **and Robert Martinuzzi**[1*]
1: Department of Mechanical and Manufacturing Engineering, University of Calgary
2500 University Dr. NW, Calgary, Alberta T2N 1N4, Canada.
*Corresponding author: rmartinu@ucalgary.ca

ABSTRACT

The wake of a cantilevered square cylinder of height-to-width ratio $h/d = 4$ protruding a thin laminar boundary layer is investigated using time-resolved stereoscopic particle image velocimetry at a Reynolds number (*Re*) of 10600. The PIV are processed using proper orthogonal decomposition (POD) and the time-domain spectral proper orthogonal decomposition (SPOD). Spectral analysis in the wake region in the vicinity of the ground plane ($z < d$) show fluctuation energy concentration centered on the vortex shedding frequency (f_s), as well as weaker contributions at 0.1, 0.4, 0.9, 1.1, and $2f_s$. It is shown that SPOD is significantly more successful than POD in separating coherent contributions within narrow spectral bandwidths and resolving spatial modes. Each of the identified frequencies is represented in a separate mode pair, which permits a better interpretation of the related dynamics. Notably, the improved modal separation assisted in associating the $0.4f_s$ spectral contribution to the interactions between the horseshoe and Kármán vortices in the wall-body junction region.

Introduction

Turbulent flows feature a wide range of spatial and temporal scales, which can represent spatially correlated coherent motions and incoherent stochastic contributions. For moderate to high Reynolds numbers ($8000 < Re = U_\infty d/\nu < 150000$, where U_∞ and ν are the free-stream velocity and kinematic viscosity, respectively), the wake of cantilevered cylinders is generally characterized by three regions along the height: (a) wall-body junction, (b) mid-height, and (c) free-end (Kawamura *et al.*, 1984; Wang *et al.*, 2006). The mid-height region is characterized by the quasi-periodic Kármán vortex shedding, whereas the other two regions are characterized by high levels of streamwise vorticity. The wall-body junction region arises due to *junction* and *horseshoe* vortices (HSV), which forms as a result of separation and roll-up of the incoming boundary layer (Ballio *et al.*, 1998), and the free-end is associated with a region of low-frequency periodicity (Kindree *et al.*, 2018; Yauwenas *et al.*, 2019). The interactions of these vortices with the Kármán vortices in the wake region of low aspect ratio cantilevered cylinders ($h/d < 10$) give rise to inter-modal dynamics (Porteous *et al.*, 2014). The present work addresses the interaction of the junction flow with the Kármán vortex shedding using time-domain SPOD of Sieber *et al.* (2016).

POD, also known as singular value decomposition or Karhunen-Loève expansion, is based on a maximization problem where a set of deterministic functions are sought which best correlate with the original data and represent it in a low-dimensional space (Sirovich, 1987; Berkooz *et al.*, 1993). POD modes are energetically optimized, which makes them well suited to capture the coherent structures (Holmes *et al.*, 2012). However, since there is no temporal constraints on the modes, a single mode can contain contributions at significantly different temporal scales.

In direct Fourier transform (DFT) or dynamic mode decomposition (DMD), introduced by Rowley *et al.* (2009) and Schmid (2010), the focus is on spanning the mode space based on fixed frequencies to identify coherent structures within narrow spectral bandwidths. In turbulent flows (e.g., shear layers or bluff body wakes), however, the coherent structures are naturally broad-band phenomena and thus difficult to represent compactly within DMD mode space.

To bridge the gap between the energetically optimal POD and the spectrally resolved DFT or DMD, Sieber *et al.* (2016) introduced a time-domain filter operation applied on the correlation matrix of POD to control the spectral bandwidth. The convolution operation of this SPOD results in better spectrally separated temporal modes. The SPOD filter length ($2N_f + 1$) can be selected, such that the decomposition sweeps the possible outcomes between the limiting cases of POD and DFT. This spectral constraint permits a better separation of phenomena that occur at multiple frequencies and energies (Sieber *et al.*, 2016).

Kindree *et al.* (2018) reported several spectral frequencies in the wake of an $h/d = 4$ square cylinder (*Re* = 10600) protruding a thin laminar boundary layer with a relative thickness of $\delta/d = 0.21$. Using POD, they associated the f_s and $2f_s$ to the Kármán vortex shedding, $f_L \approx 0.1f_s$ to the low frequency signature from the free-end, and the $f_{ai} = f_s \pm f_L$ ($i = 1$ and 2) (named as accompanying frequencies) to the interactions between the free-end and Kármán vortices. In addition, they reported frequency peaks around $0.345f_s$ just above the ground plane, which were attributed to primary HSV system instabilities (Baker, 1979). However, using POD, challenges emerged in separating dynamics in the junction region where the HSV, junction, and Kármán vortices interacted. Specifically, a broadband spectral concentration around $0.4f_s$ was observed. The energy was distributed over several modes containing significant spectral energy contributions at other frequencies.

This study presents a further analysis of the PIV data in the junction region of the same square cylinder case. The aim is to discuss the benefits of using SPOD to separate dynamics. The low-order representation using SPOD provides a more interpretable basis to explain the physical phenom-

ena and relation between different vortical structures and dynamics, especially between HSV and Kármán vortices.

Experimental Setup

Figure 1 presents the schematics of a cantilevered $h/d = 4$ square cylinder protruding a thin laminar boundary layer, investigated experimentally at an inlet free-stream velocity of $U_\infty = 14.3$ m/s (corresponding to $Re = 10600$). The square cylinder was machined aluminum mounted on a machined-flat rigid steel ground plate with a 4:1 elliptical leading edge (minor axis matching the plate thickness). The intersection of the cylinder central axis with the plate marks the origin of the Cartesian coordinate system: x, y, and z denote streamwise, lateral, and spanwise directions with u, v, and w being the corresponding velocity components. All coordinate variables and velocity components are non-dimensionalized by d and U_∞, respectively. The laminar boundary layer developed naturally and reached a thickness of $\delta/d = 0.21$ ($\delta/h = 0.053$) at the location of the obstacle with the obstacle removed. The free stream turbulence was measured to be less than 0.1%.

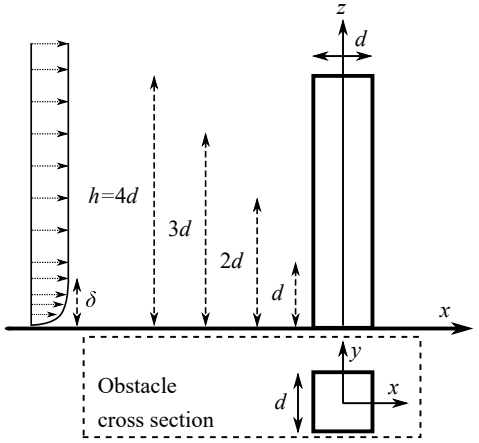

Figure 1. Schematics of the experimental set-up in the test section of the wind tunnel (not drawn to scale) with the coordinate system and related nomenclature.

The velocity fields were measured with time-resolved stereoscopic particle image velocimetry (PIV). A *LaVision FlowMaster* system was used for PIV measurements, which were run in a high inlet contraction (area ratio 36:1) open-test-section suction wind tunnel, described in details in Kindree *et al.* (2018), for which the free stream pressure gradient is zero. To ensure statistical convergence of the first and second statistical moments and POD/ SPOD modes, $N \approx 15000$ snapshots were acquired in each plane.

Analytical Methodology

Following Hussain (1983), the velocity field, $\boldsymbol{u}(\boldsymbol{x},t)$, is subject to a triple decomposition, into a mean, $\boldsymbol{U}(\boldsymbol{x})$, and coherent and incoherent contributions ($\boldsymbol{u}_c(\boldsymbol{x},t)$ and $\boldsymbol{u}^{''}(\boldsymbol{x},t)$, respectively):

$$\boldsymbol{u}(\boldsymbol{x},t) = \boldsymbol{U}(\boldsymbol{x}) + \underbrace{\boldsymbol{u}_c(\boldsymbol{x},t) + \boldsymbol{u}^{''}(\boldsymbol{x},t)}_{\boldsymbol{u}^{'}(\boldsymbol{x},t)} \tag{1}$$

where $\boldsymbol{u}^{'}$ represents the total fluctuations. Upright bold symbols indicate vectors and $\boldsymbol{x}$ and t represent position and time, respectively. The POD and SPOD are used to determine the coherent contributions. For completeness, a brief overview of these methods are given below. The POD is defined as:

$$\boldsymbol{u}_c(\boldsymbol{x},t) = \sum_{i=1}^{N} a_i(t)\phi_i(\boldsymbol{x}) \tag{2}$$

where a_i and ϕ_i are the temporal and spatial modal functions. At each PIV plane, the correlation, $\boldsymbol{R}$, between two snapshots, $\boldsymbol{u}(\boldsymbol{x})$ and $\boldsymbol{v}(\boldsymbol{x})$, is calculated through an inner product $\langle .,. \rangle$:

$$\langle \boldsymbol{u}(\boldsymbol{x}), \boldsymbol{v}(\boldsymbol{x}) \rangle = \int_A \boldsymbol{u}(\boldsymbol{x})\boldsymbol{v}(\boldsymbol{x})\mathrm{dxdy} \tag{3}$$

where A specifies the spatial region (each PIV plane) over which the correlation is integrated. The elements of $\boldsymbol{R}$ are given by:

$$R_{i,j} = \frac{1}{N}\langle \boldsymbol{u}^{'}(\boldsymbol{x},t_i), \boldsymbol{u}^{'}(\boldsymbol{x},t_j) \rangle \tag{4}$$

$\boldsymbol{R}$ is an $N \times N$ real symmetric positive-definite matrix; therefore, it's eigenvectors, a_i, are orthogonal to each other. a_i and their corresponding eigenvalues, λ_i, represent the temporal modes and their energies, respectively, and are both sorted in a descending order. In addition, a_i are scaled with the energy of single modes.

$$\frac{1}{N}(a_i, a_j) = \lambda_i \delta_{ij} \qquad \mathrm{TKE} = \frac{1}{2}\sum_{i=1}^{N} \lambda_i \tag{5}$$

where (.,.) represents the scalar product and TKE is the total kinetic energy of the fluctuations. Finally, the spatial modes are obtained from projecting each fluctuating snapshot ($\boldsymbol{u}_i^{'}$) onto its corresponding a_i:

$$\phi_i(\boldsymbol{x}) = \frac{1}{N\lambda_i}\sum_{j=1}^{N} a_i(t_j)\boldsymbol{u}^{'}(\boldsymbol{x},t_j) \tag{6}$$

The POD spatial modes are orthonormal by construction: $\langle \phi_i, \phi_j \rangle = \delta_{ij}$.

In the SPOD method proposed by Sieber *et al.* (2016), the aim is to enforce diagonal similarity of the correlation matrix. This is achieved by operating a low-pass filter along the diagonals of $\boldsymbol{R}$. The elements of the filtered correlation matrix, $\boldsymbol{S}$, are given by:

$$\boldsymbol{S}_{i,j} = \sum_{k=-N_f}^{N_f} g_k \boldsymbol{R}_{i+k,j+k} \tag{7}$$

where g is a symmetric finite impulse response filter with a length of $2N_f + 1$. $\boldsymbol{S}$ converges to a symmetric Toeplitz matrix if the filter length extends over the entire time series.

The rest of the procedure of SPOD is the same as for POD. The temporal modal coefficients remain orthogonal, but the spatial modes are no longer orthogonal. The TKE is still represented with the same definition, however, less energy will be recovered compared to POD by the first modes. However, similar to POD, if all SPOD modes are used for reconstruction, the flow field is recovered. For a more comprehensive discussion on SPOD, readers are referred to Sieber *et al.* (2016).

Results and Discussion

Figure 2(a),(b) shows the schematics of a typical laminar HSV system at (a) $y = 0$ (symmetry plane) and (b) $x-y$ plane close to the base plate. Figure 2(c) shows the mean surface flow patterns from oil-film visualization experiments of Kindree *et al.* (2018) on the ground plane. The incoming boundary layer initially separates along L_1, the foremost point of which is the separation saddle point, S. The topology of the HSV system consists of large primary (PV) and corner (CV) vortices and small secondary vortices (SV). The interaction of the CV and obstacle generally gives rise to a corner junction vortex (JV) and the interactions of the CV and PV with the wall give rise to small counter-rotating vortices near the wall (BAV_1 and BAV_2, respectively). The dashed lines, L_1, L_2, and L_3, are separation lines associated with SV, BAV_2 and BAV_1, respectively, and L_4 is related to JV. As the PV and CV stretch and extend laterally from the symmetry plane, the trajectory of their cores follow L_2 and L_3.

The HSV system is linked to significant unsteady dynamics. Baker (1979, 1991) categorized the behavior of HSV systems into four regimes based on the boundary layer displacement thickness (δ^*): (i) non-oscillatory, (ii) low frequency secondary oscillations associated with the entire HSV system ($f^*\delta^*/U$ = 0.01; f^* being the dimensional oscillation frequency), (iii) high frequency primary oscillations associated with the instability of PV ($0.07 < f^*(\delta^* d)^{0.5}/U_\infty < 0.09$), and (iv) turbulent. The present laminar boundary layer case corresponds to the third category. In the wake, frequency peaks around $f = 0.345$ (corresponding to $f^*(\delta^* d)^{0.5}/U_\infty = 0.093$) were reported in the velocity fluctuation spectra in regions corresponding to the left corner of the PIV plain in Fig. 2(c), which were attributed to primary oscillation instability of the HSV system (Kindree *et al.*, 2018).

Figure 3 shows the power spectral density function (PSDF) of fluctuating velocity components (u' and v') at various locations at $z = 0.11$, selected strategically based on an initial grid search. All frequencies reported earlier by Kindree *et al.* (2018) can be seen in these spectra (f_{ai} cannot be easily discerned). In addition, a broader band accumulation of energy around $f_h = 0.4 f_s$ is observed at $(3.8, 0.8)$, $(4.1, 1.1)$, and $(4.8, 1.6)$ points, all of which lie along the pigment line indicated by the green arrows (between L_2 and L_3 lines) in Fig. 2(c). Although this hump of energy is difficult to discern due to its proximity to f_s, its significance will be discussed in considering the SPOD decomposition.

To provide a clearer interpretation of the dynamics associated with each frequency, an illustrative comparison of results obtained from the POD and SPOD of the velocity field data is provided for the $z = 0.11$ plane in the cylinder wake. In the case of SPOD, several filter lengths ($N_f = 0.8/f_s$ to $25.6/f_s$) were considered. As N_f increases, better separation of frequencies in PSDF and more refined spatial distributions are obtained. However, this comes at the penalty of retaining less TKE with the first modes. Here, $N_f = 6.4/f_s$ was selected to provide the optimum balance between spectral separation and not losing significant portions of TKE. Following Holmes *et al.* (2012), a symmetric/ antisymmetric split was carried out on the dataset prior to performing the decomposition to accelerate the convergence in terms of PIV snapshots needed.

Figure 4 illustrates the u and v components of selected spatial modes obtained using POD (columns 1 and 2) and SPOD (columns 4 and 5). To the right of each set, the PSDF of the corresponding temporal modal coefficients are shown. For POD, rows 1 to 3 present the first, third, and fifth most energetic antisymmetric modes (ϕ_{a1}, ϕ_{a3}, and ϕ_{a5}, respectively) and rows 4 to 6 present the first three most energetic symmetric modes (ϕ_{s1} to ϕ_{s3}, respectively). For better visualization, the SPOD modes are presented based on their resemblance to the presented POD modes (with respect to both spatial distribution and spectral behavior). In both antisymmetric and symmetric fields, only the first mode of a harmonic pair is shown for brevity.

For POD, the first two antisymmetric modes (ϕ_{a1} and ϕ_{a2}) are associated to Kármán vortex shedding, with a sharp frequency peak at $f_s = 120$ Hz ($St = f_s d/U_\infty = 0.11$). The other frequencies (f_h, f_{ai}, and $2f_s$) can also be seen in the PSDF. However, these frequencies either appear in several modes or together in the same modes, which makes the interpretation of the spatial modes difficult. For instance, the POD modes most closely corresponding to f_{ai} are the (ϕ_{a5}, ϕ_{a6}) mode pair. However, energetic contents corresponding to these frequencies can also be seen in the spectra of ϕ_{a1} to ϕ_{a4}. On the other hand, the temporal spectra of ϕ_{s2} shows an accumulation of energy around both f_L and f_h as well as the sharp spectral peak of $2f_s$.

By applying a filter to the correlation matrix, SPOD allows separation of these frequencies and provides a more interpretable basis. For instance, in the antisymmetric field, f_s and f_{ai} are clearly separated: the (ϕ_{a1}, ϕ_{a2}) mode pair corresponds to f_s and (ϕ_{a3}, ϕ_{a4}) corresponds to f_{ai}. The f_h is also better resolved with SPOD. Compared to the spectra of (ϕ_{a3}, ϕ_{a4}) POD mode pair, the spectra of (ϕ_{a5}, ϕ_{a6}) SPOD mode pair contains significantly less energetic contents on either sides of f_h. Accordingly, the spatial distribution is better resolved and the coherent motion associated with f_h can be differentiated from that of the shed structures.

The better resolved spatial distribution of the (ϕ_{a5}, ϕ_{a6}) SPOD mode pair allows for a comparison with the oil-film visualization. Maximum magnitude of the spatial Eigenfunction for the u component are aligned along the dark pigment lines, indicated by green arrows in Fig. 2(c). This is consistent with the energetic contents observed around f_h in the spectra of Fig. 3. Preliminary analysis of SPOD results at higher planes ($z < 0.5$) show similar patterns, where the f_h gradually weakens with height such that at $z = 0.5$, it is no longer detected. Hence, the modes associated with f_h are expressed in the region close to the ground plane where the HSV downstream extensions are in the proximity of the shed vortices. This suggests that the f_h is related to the perturbation of the downstream extensions of the HSV system.

The energetic contents around f_h in the spectra of the (ϕ_{s5}, ϕ_{s6}) SPOD mode pair is more clearly separated compared to the POD modes. The frequency and spatial distribution of this mode pair resemble the ones of the (ϕ_{a5}, ϕ_{a6}) SPOD mode pair, suggesting a connection with the primary HSV system instabilities. However, when recon-

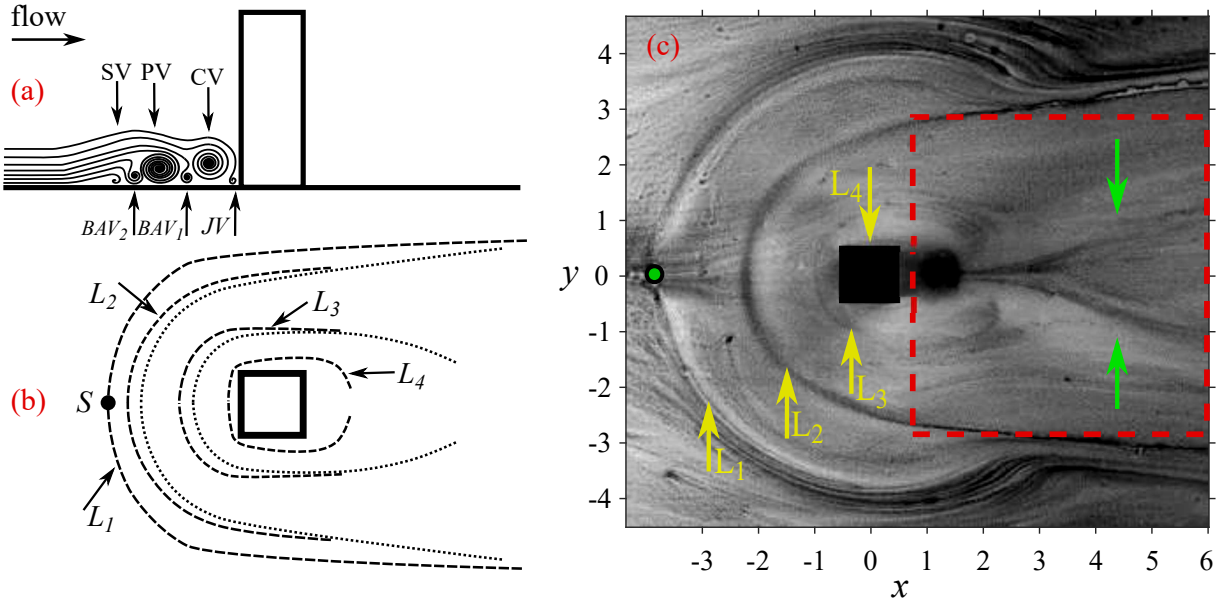

Figure 2. Left side: schematics of a typical laminar horse-shoe votex (HSV) system: (a) side view and (b) top view (sketch inspired by earlier studies: Baker (1979); Simpson (2001); Lin *et al.* (2002); Kirkil & Constantinescu (2012); Martinuzzi & Tropea (1993); Seal *et al.* (1997); Ballio *et al.* (1998), and not drawn to scale. Vortices are named following Kirkil & Constantinescu (2012)). Right side: oil-film visualization of the flow patterns on the ground plate overlaid with the PIV window (red dashed-lines). Figure is reprinted with permission from Kindree *et al.* (2018).

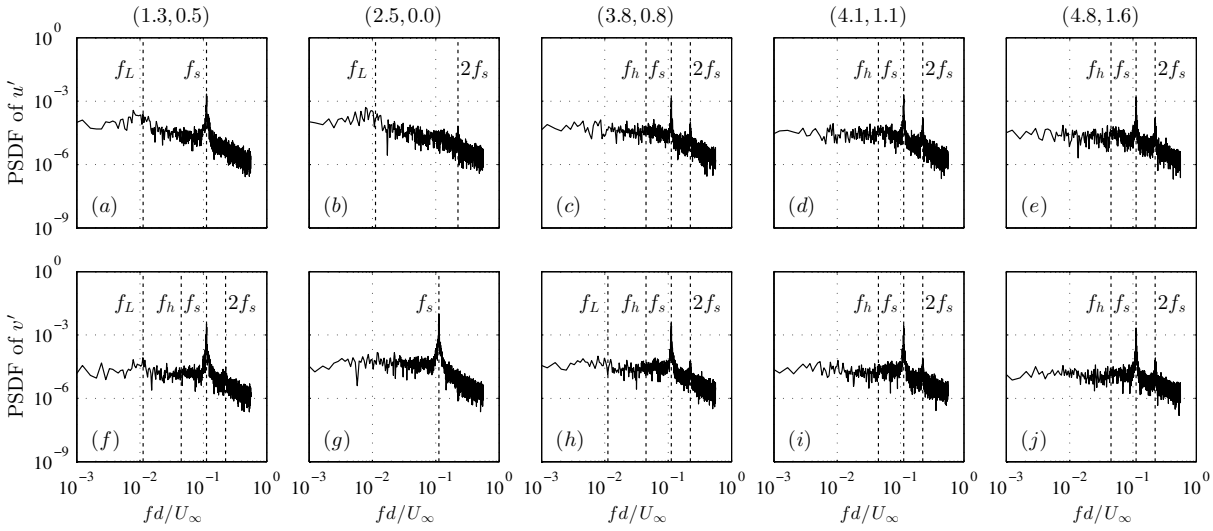

Figure 3. Power spectral density functions (PSDF) of u and v fluctuating velocity components (first and second rows, respectively). (a),(f) at $(1.3, 0.5)$; (b),(g) at $(2.5, 0.0)$; (c),(h) at $(3.8, 0.8)$; (d),(i) at $(4.1, 1.1)$; and (e),(j) at $(4.8, 1.6)$.

structing the velocity fields using these mode pairs, the vortical structures appears convective with the antisymmetric pair, but not with the symmetric one. This suggests that each mode pair captures different aspects of interaction between the primary vortices of the HSV system and Kármán vortices in the junction region ($z \leq 1$).

The other spectral peaks and related dynamics (i.e., f_L and $2f_s$) in the symmetric field is also better resolved using SPOD. With POD, except ϕ_{s1}, which shows a clear spectral peak around f_L, the spectra of next five modes (ϕ_{s2} to ϕ_{s6}) exhibit energetic contents around multiple frequencies (i.e., f_L, f_h, f_s, and $2f_s$; ϕ_{s4} to ϕ_{s6} are not shown for brevity). ϕ_{s4} and ϕ_{s5} show energetic contents around f_L, f_s, and $2f_s$, while ϕ_{s6} shows energetic contents around f_L and f_s. With SPOD, however, energetic contributions at f_L, f_h, and $2f_s$ appear in separate mode pairs: (ϕ_{s1}, ϕ_{s2}) contain energetic contributions at f_L, (ϕ_{s3}, ϕ_{s4}) at $2f_s$, and (ϕ_{s5}, ϕ_{s6}) at f_h.

The low frequency f_L has been associated with the flapping instability of the separated shear layers from the free-end (Kindree *et al.*, 2018; Yauwenas *et al.*, 2019). At the $z = 0.11$ plane, this flapping motion is mainly represented by the (ϕ_{s1}, ϕ_{s2}) SPOD mode pair and accounts for 2.8% of TKE. The u component appears most energetic (representing 2.1% of TKE vs. 0.5% and 1% with the v and w components, respectively). The spatial modal function for u indicates that high contributions due to this mode are concentrated along the edge of the recirculation region - i.e., along the shear layer. The SPOD analysis of higher planes shows that the relative TKE contribution related to f_L increases with height. The w component becomes more

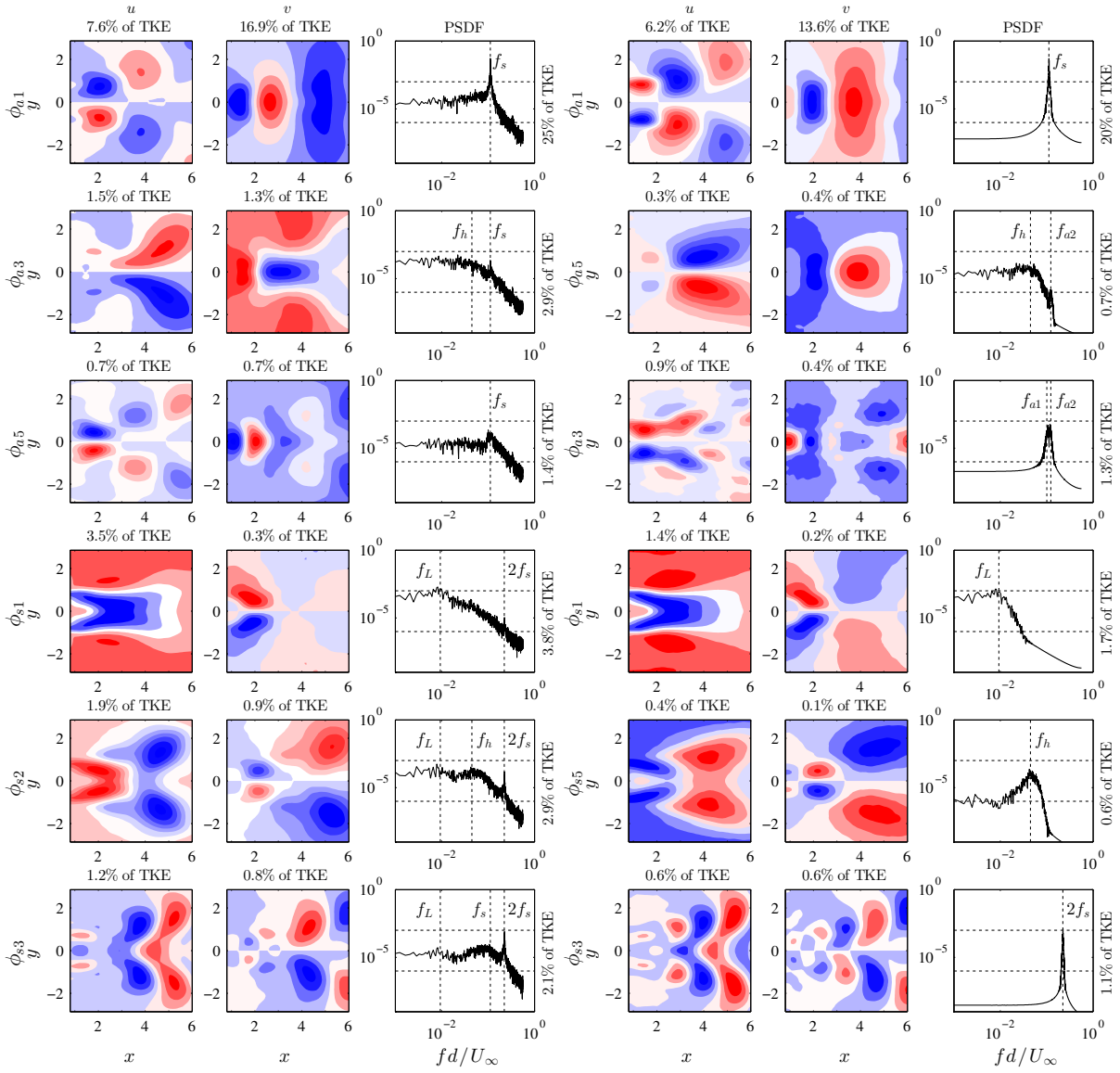

Figure 4. Decomposition of the velocity field. Spatial modal functions for u and v, and PSDF from POD (left three columns) and SPOD with a filter length of $N_f = 6.4/f_s$ (right three columns). For POD: ϕ_{a1}, ϕ_{a3}, and ϕ_{a5} represent the first, third, and fifth most energetic antisymmetric and ϕ_{s1}, ϕ_{s2}, and ϕ_{s3} represent the first, second, and third symmetric modes. For SPOD: the modes most similar to the selected POD modes with regards to their spatial distributions and spectral patterns are shown (i.e., ϕ_{a1}, ϕ_{a5}, and ϕ_{a3} for the antisymmetric modes, and ϕ_{s1}, ϕ_{s5}, and ϕ_{s3} for the symmetric modes).

significant towards the mid-span height due to the intensified downwash effects. Hence, the observed behavior of this mode is consistent with the shear layer flapping instability.

Figure 5 shows the phase portraits of select temporal modes using POD (first row) and SPOD (second row). The trajectories obtained in the phase space with SPOD show a clearer relationship between temporal modes: in a_{a1} vs. a_{a2}, the cyclical relationship between the two legs of a harmonic pair is better resolved; in a_{a1} vs. a_{a4} (also in a_{a1} vs. a_{a3}), a clearer bi-modal behavior, which corresponds to f_{a1} and f_{a2}, can be identified. In considering a_{a1} vs. a_{s1}, the parabolic relationship between the shedding strength and the slow base flow variation, described by Noack *et al.* (2003), is more clearly rendered. Finally, in a_{a1} vs. a_{s3} and a_{a1} vs. a_{s4}, clear Lissajou portraits are seen, which indicate that the phase dynamics of the $2f_s-$harmonic are enslaved to the fundamental harmonic (Bourgeois *et al.*, 2013).

Conclusion

A comparative study is done on the ability of POD and SPOD techniques in separating dynamics and providing a more interpretable basis to study them in the wake of an $h/d = 4$ cantilevered square cylinder. It was shown that SPOD can effectively (i) separate vortical structures within narrow spectral bandwidth without significant losses of TKE presentation, (ii) pair similar modes, and (iii) deliver more clearly resolved phase relationships between temporal modes, which allow a clearer representation of the flow dynamics and nonlinear interactions. In particular to the presented case, SPOD successfully separated a broad band energy distribution around $f_h = 0.4f_s$, which was not possible with POD. The comparison of the more refined related spatial modes and the oil-film visualization flow patterns on the ground plate assisted in associating this frequency to perturbations of the downstream extensions of the HSV due to interactions with the Kármán vortices.

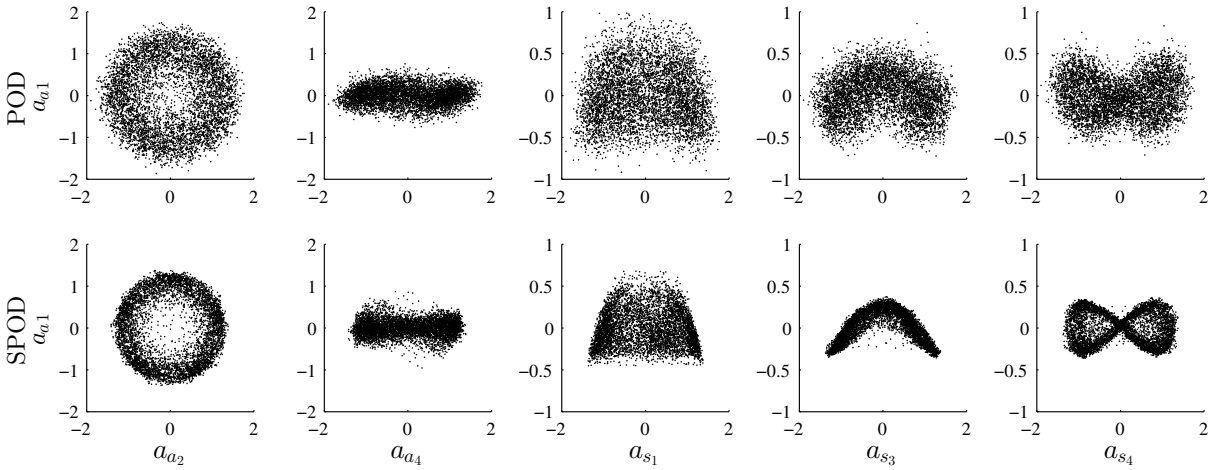

Figure 5. Phase portrait of select temporal modes obtained from POD (top row) and SPOD (bottom row): a_{a1} vs. a_{a2}, a_{a4}, a_{s1}, a_{s3}, and a_{s4}. Every second point is plotted.

REFERENCES

Baker, C. J. 1979 The laminar horseshoe vortex. *Journal of Fluid Mechanics* **95** (2), 347–367.

Baker, C. J. 1991 The oscillation of horseshoe vortex systems. *Journal of Fluids Engineering* **113**, 489–495.

Ballio, F., Bettoni, C. & Franzetti, S. 1998 A survey of time-averaged characteristics of laminar and turbulent horseshoe vortices (Data Bank Contribution). *Journal of Fluids Engineering* **120**, 233–242.

Berkooz, G., Holmes, P. & Lumley, J. L. 1993 The proper orthogonal decomposition in the analysis of turbulent flows. *Annual Review of Fluid Mechanics* **25** (1), 539–575.

Bourgeois, J. A., Noack, B. R. & Martinuzzi, R. J. 2013 Generalized phase average with applications to sensor-based flow estimation of the wall-mounted square cylinder wake. *Journal of Fluid Mechanics* **736**, 316–350.

Holmes, P., Lumley, J. L., Berkooz, G. & Rowley, C. W. 2012 *Turbulence, coherent structures, dynamical systems and symmetry*.

Hussain, A. K. M. F. 1983 Coherent structures - reality and myth. *Physics of Fluids* **26** (10), 2816–2850.

Kawamura, T., Hiwada, M., Hibino, T., Mabuchi, I. & Kumada, M. 1984 Flow around a finite circular cylinder on a flat plate. *Bulletin of JSME* **27** (232), 2142–2151.

Kindree, M. G., Shahroodi, M. & Martinuzzi, R. J. 2018 Low-frequency dynamics in the turbulent wake of cantilevered square and circular cylinders protruding a thin laminar boundary layer. *Experiments in Fluids* **59:186**, 1–26.

Kirkil, G. & Constantinescu, G. 2012 A numerical study of the laminar necklace vortex system and its effect on the wake for a circular cylinder. *Physics of Fluids* **24** (7), 073602(1–25).

Lin, C., Chiu, P. H. & Shieh, S. J. 2002 Characteristics of horseshoe vortex system near a vertical plate-base plate juncture. *Experimental Thermal and Fluid Science* **27**, 25–46.

Martinuzzi, R. J. & Tropea, C. 1993 The flow around surface-mounted, prismatic obstacles placed in a fully developed channel flow (Data Bank Contribution). *Journal of Fluids Engineering* **115**, 85–92.

Noack, B. R., Afanasiev, K., Morzynski, M., Tadmor, G. & Thiele, F. 2003 A hierarchy of low-dimensional models for the transient and post-transient cylinder wake. *Journal of Fluid Mechanics* **497**, 335–363.

Porteous, R., Moreau, D. J. & Doolan, C. J. 2014 A review of flow-induced noise from finite wall-mounted cylinders. *Journal of Fluids and Structures* **51**, 240–254.

Rowley, C. W., Mezic, I., Bagheri, S., Schlatter, P. & Henningson, D. S. 2009 Spectral analysis of nonlinear flows. *Journal of Fluid Mechanics* **641**, 115–127.

Schmid, P. J. 2010 Dynamic mode decomposition of numerical and experimental data. *Journal of Fluid Mechanics* **656**, 5–28.

Seal, C. V., Smith, C. R. & Rockwell, D. 1997 Dynamics of the vorticity distribution in endwall junctions. *AIAA Journal* **35** (6), 1041–1047.

Sieber, M., Paschereit, C. O. & Oberleithner, K. 2016 Spectral proper orthogonal decomposition. *Journal of Fluid Mechanics* **792**, 798–828.

Simpson, R. L. 2001 Junction flows. *Annual Review of Fluid Mechanics* **33**, 415–443.

Sirovich, Lawrence 1987 Turbulence and the dynamics of coherent structures. III. Dynamics and scaling. *Quarterly of Applied Mathematics* **45** (3), 583–590.

Wang, H. F., Zhou, Y., Chan, C. K. & Lam, K. S. 2006 Effect of initial conditions on interaction between a boundary layer and a wall-mounted finite-length-cylinder wake. *Physics of Fluids* **18** (6), 065106(1–12).

Yauwenas, Y., Porteous, R., Moreau, D. J. & Doolan, C. J. 2019 The effect of aspect ratio on the wake structure of finite wall-mounted square cylinders. *Journal of Fluid Mechanics* **875**, 929–960.